Received: Added at production | Revised: Added at production | Accepted: Added at production

DOI: xxx/xxxx

ARTICLE TYPE

Implementation of a new strain split to model unilateral contact within the phase field method

Thanh-Tung Nguyen*[1] | Julien Yvonnet[2] | Danièle Waldmann[1] | Qi-Chang He[2]

[1]University of Luxembourg, Laboratory of Solid Structures, 6, Rue Richard Coudenhove-Kalergi, L-1359, Luxembourg
[2]Université Paris-Est, Laboratoire Modélisation et Simulation Multi Échelle MSME UMR 8208 CNRS, 5 bd Descartes, F-77454 Marne-la-Vallée, France

Correspondence
*Thanh-Tung Nguyen. Email: thanh-tung.nguyen@uni.lu

Summary

A new orthogonal split of strain tensor into compressive and tensile parts is implemented within the phase field model to mimic unilateral contact condition with which any existing cracks and any crack propagation have to comply. The resulting phase field model offers several advantages as compared to other available schemes. First, it involves rigorous orthogonality between traction and compression parts. Second, it yields remarkably simple, new analytical expressions of the projectors which provide computational saving during the crack propagation simulation. Finally, it can be applied to arbitrary initial elastic anisotropic media, which is not the case of other available strain tensor split operators. A detailed comparison of the fracture responses predicted by the present model and other approaches is provided. It is shown that the present orthogonal decomposition is able to accurately predict experimental results and removes spurious effects found in other schemes for specific loads like compression.

KEYWORDS:
Fracture, Phase field model, Spectral decomposition, Anisotropy, Unilateral contact condition

1 | INTRODUCTION

The phase field method (PFM) is nowadays one of the most robust and efficient numerical tool to study brittle and ductile fractures. It has been introduced based on the pioneer works on variational approaches to fracture by Francfort, Marigo and their co-authors [1,2,3]. The technique makes use of a regularized description of discontinuities through an additional phase field variable and strongly alleviates meshing problems for describing brittle/ductile cracking. Furthermore, the PFM can effectively handle the phenomena of crack nucleation, interaction and arbitrary crack morphologies. This method has been successfully applied to model complex, multiple crack fronts, and branching in both 2D/3D without ad-hoc numerical treatments, see e.g. [4,5,6,7,8,9,10,11].

In the phase field model, as in classical damage models, avoiding material interpenetration in the contact of the lips of any crack is performed by decomposing the strain density function and by introducing a dependence on damage via the so-called "traction" or "positive" part. Many efforts have been made in the context of damage models to overcome somehow unrealistic tension-compression symmetry in the failure models. For instance, Ortiz et al. [12] introduced a split decomposition of strain energy based on the positive/negative parts of the stress tensor which can accommodate fully anisotropic elastic degradation. This decomposition has been adapted in many studies, such as Simo and Ju [13], and Mazars and co-authors [14,15,16,17,18], wherein a simplified formulation of a volumetric tensile strain projection was introduced. Cervera et al. [19] proposed a biaxial effective principal stress space, in which the equivalent stress is defined to govern the damage evolution. Comi and Perego [20] developed a bi-dissipative damage model to describe tension and compression behavior independently. In the mentioned work, the unilateral

effects were modeled by splitting the volumetric strain energy into two parts: one depending on the positive part of the trace of strains, affecting both tension/compression damage variables, and a second part depending on the negative part of the trace of strains, only affecting the compression damage. Giacomini and Ponsiglione[21] introduce a geometrically non-linear model where the non-interpenetration condition appears as a non-local constraint. Wu and Cervera[22] proposed a new positive/negative projection operator in energy norm to ensure that the secant stiffness tensor always possesses major symmetry and exhibits orthotropic behavior under uniaxial tension and mixed tension/compression. More recently, He and Shao have proposed a new orthogonal decomposition of the strain tensor to model the unilateral effects within the crack lips[23].

Some of the mentioned ideas have been incorporated into the phase field model[24,25,26,5,27,8,28]. For instance, Amor et al.[5] adopted a model based on the volumetric/deviatoric spectral decomposition of the strain tensor and assumed that damage is created by expansion and shear. The extensive/compressive spectral decomposition of the strain tensor used by Miehe et al.[8] is another popular formulation. As noticed in[10,28], the difference between these two models becomes evident in a situation where all three principal strains are negative. In this case, according to[5], the deviatoric strain energy is always degraded, and the related phase-field model will produce cracking in the corresponding regions while the model in[8] will not. This, however, provides a significant difference in fracture behavior. The one proposed by Amor et al.[5] seems to be better in terms of numerical efficiency, but as shown in the numerical examples of the present paper, their formulation introduces spurious effects and some problems in simulating crack propagation under compression loads. The formulation proposed by Miehe et al.[8] has demonstrated to be robust in these situations, but requires a higher computation cost due to the evaluation of eigenvalues and eigenvectors of the strain tensors at each load increment. Moreover, the spectral decomposition proposed by Miehe et al.[8] does not satisfy the orthogonal condition of the extensive and compressive parts[29]. Another model has been proposed by Freddi et al.[27], with the assumption that the fracture is only due to the deviatoric part of the strain tensor. This model suitable for compressed materials, becomes incorrect in expanded regions where fracture due to tensile strains is expected[5].

In this study, we use and implement a recent new formulation of the orthogonal decomposition of the strain tensor proposed by He and Shao[23] in the phase field method. As in the work of Miehe[8], this formulation is based on the spectral decomposition of the strain tensor into extensive (positive) and compressive (negative) parts. However, the main difference with the model of Miehe[8] is that the extensive and compressive parts of the strain tensors are here rigorously orthogonal in the sense of an inner product, and both fourth-order elastic stiffness and compliance tensors act as metric tensors. Two projection tensors following the idea of Miehe[30] are also introduced to numerically implement the new model within the Finite Element framework in an efficient manner. Remarkably, very simple, closed forms expressions can be analytically obtained for these projectors leading to a very efficient scheme. A staggered scheme is proposed in this context, which has the consequence that each problem to be solved at each load step remains linear, the calculation of eigenvalues being reported to the previous iteration of the algorithm, as in[11]. Another important advantage of the present model is that it can be applied to any initial elastic anisotropy, in contrast with other available models which are restricted to special classes of anisotropy. For instance, there is no available formulation for modeling anisotropic materials within the framework proposed by Miehe et al.[8]. The model proposed by Amor et al.[5] requires the definition of the bulk modulus[31,32]. Hence, it can only handle some simple anisotropic materials (cubic, hexagonal,...). We provide a careful comparison with other available models for the fracture behavior under different load testing scenarios, e.g., shear, traction, and compression and illustrate the capability of the method to handle cracking in anisotropic elastic media.

This paper is organized as follows. A brief review of the phase field for fracture and a description of the new formulation of the orthogonal decomposition of the strain tensor in this context are given in section 2. In section 3, the numerical implementation details of the present scheme are provided. In the Section 4, several numerical experiments are presented to validate and illustrate the capabilities of the proposed framework.

2 | PHASE FIELD METHOD WITH THE NEW ORTHOGONAL STRAIN SPLIT OPERATOR

2.1 | Brief review of the phase field method

We consider a cracked body $\Omega \subset \mathbb{R}^D$, with D the space dimension and $\partial\Omega$ its boundary. Let Γ be a manifold of dimension $D-1$ representing crack discontinuity within Ω, see Fig. 1(a). The total energy of the cracked body in accordance with Griffith's theory of brittle fracture can be defined by

$$E = \int_{\Omega} \psi^e(\boldsymbol{\varepsilon}) \, \mathrm{d}\Omega + \int_{\Gamma} g_c \, \mathrm{d}S, \tag{1}$$

where ψ^e is the elastic energy density, $\boldsymbol{\varepsilon} = \frac{1}{2}\left(\nabla\mathbf{u} + \nabla\mathbf{u}^{\mathrm{T}}\right)$ is the infinitesimal strain tensor, and g_c describes the critical fracture energy.

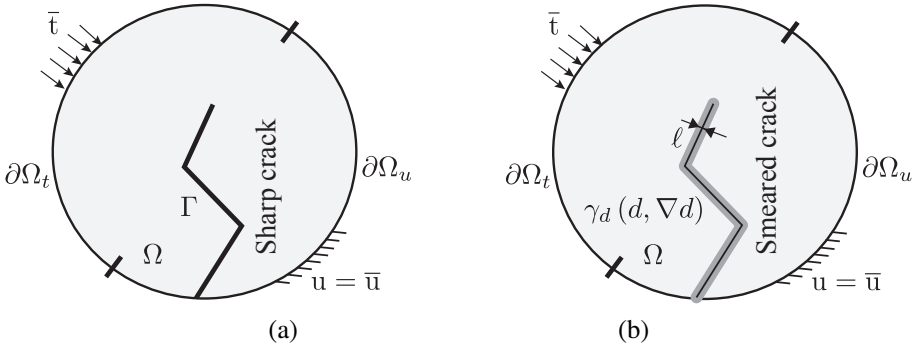

FIGURE 1 Regularized representation of a crack: (a) sharp crack model; (b) regularized representation through phase field.

In a regularized framework[33], the crack geometry Γ is approximated by a smeared representation, which can be set as a function of a phase field, $d(\mathbf{x}) \in [0, 1]$. This scalar parameter $d(\mathbf{x})$ takes a unit value on Γ and vanishes away from it. The phase field is here associated with the damage level: $d = 1$ represents the fully broken material while $d = 0$ is the sound state of the material. The fracture energy can be approximated accordingly by:

$$\int_{\Gamma} g_c \, \mathrm{d}S \simeq \int_{\Omega} g_c \gamma_d(d, \nabla d) \, \mathrm{d}\Omega. \tag{2}$$

Above, γ_d is considered as the crack surface density function. A second-order expression for γ in a 3D context can be expressed as (see e.g.[8,34])

$$\gamma_d(d, \nabla d) = \frac{3}{8\ell} d + \frac{3\ell}{8} \nabla d \cdot \nabla d, \tag{3}$$

in which ℓ is a regularized length describing the thickness of the smeared crack. As discussed in[3,34], this approximation satisfies the $\Gamma-$convergence condition, i.e., the solution of the regularized scheme converges to the solution of the sharp crack description when ℓ goes to zero. It should be mentioned that ℓ is also an internal parameter that affects the critical stress of the crack initiation. Discussions on how to choose this parameter for practical situations can be found e.g. in[5,10,35,36].

Within the regularized description of crack, the total energy form in (1) can be rewritten as

$$E = \int_{\Omega} \psi^e\left(\boldsymbol{\varepsilon}, d\right) \, \mathrm{d}\Omega + \int_{\Omega} g_c \gamma_d(d, \nabla d) \, \mathrm{d}\Omega. \tag{4}$$

The phase field d is incorporated into the strain energy $\psi^e\left(\boldsymbol{\varepsilon}, d\right)$ to account for the loss of material stiffness in the failure zone. It is often done through the use of the degradation function $g(d) = (1 - d)^2 + \epsilon$ (with $\epsilon \ll 1$, satisfying $g(0) \approx 1$, $g(1) \approx 0$ and $g'(1) = 0$, see[2,8]). In the phase field model, unilateral contact condition for any crack is obtained by splitting the elastic strain density function tensor into a damaged part ψ^{e+} associated to damage and a part ψ^{e-} which does not activate damage. This implies the following expression of the strain energy

$$\psi^e(\boldsymbol{\varepsilon}, d) = g(d)\, \psi^{e+}\left(\boldsymbol{\varepsilon}\right) + \psi^{e-}\left(\boldsymbol{\varepsilon}\right). \tag{5}$$

Several studies have been conducted to provide an appropriate formulation for $\psi^e(\boldsymbol{\varepsilon}, d)$. Two popular models are: (a) the one of Amor et al.[5] denoted here by (SD1) and (b) that of Miehe et al.[8] hereby noted (SD2). The main ideas of these two schemes are reviewed in A.

2.2 | Phase field model with an orthogonal decomposition of the strain tensor into compressive/tensile parts

Alternatively to the formulation used in Amor et al.[5] and Miehe et al.[8], we adopt here a new decomposition scheme recently proposed by He and Shao[23] (denoted here by (SD3)). This scheme is based on the decomposition of the strain tensor into two complementary parts, which are orthogonal in the sense of an inner product where the fourth-order elastic stiffness tensor acts as the metric operator. Let $\mathbb{C}$ be the fourth-order stiffness tensor, the traction part (denoted by $(.)^+$) and compression part (denoted by $(.)^-$) of the strain energy density are expressed by

$$\psi^{e\pm}(\boldsymbol{\varepsilon}) = \frac{1}{2}\left[\boldsymbol{\varepsilon}^{\pm} : \mathbb{C} : \boldsymbol{\varepsilon}^{\pm}\right]. \tag{6}$$

In this formulation, the traction/compression elastic strain energy parts depend explicitly on a generic form of the stiffness tensor $\mathbb{C}$. This implies that the present model can be applied to arbitrary anisotropic elastic behavior.

The orthogonality condition for the positive/negative parts $\boldsymbol{\varepsilon}^{\pm}$ is specified by

$$\boldsymbol{\varepsilon}^{+} : (\mathbb{C} : \boldsymbol{\varepsilon}^{-}) = \left(\mathbb{C} : \boldsymbol{\varepsilon}^{+}\right) : \boldsymbol{\varepsilon}^{-} = 0. \tag{7}$$

The requirement in Eq. (7) can be ensured through a method based on the elastic energy preserving transformation proposed by He and co-author[37,23]. The main idea of this method is summarized below. First, the square root of the elastic stiffness tensor is introduced

$$\mathbb{C}^{1/2} = \sum_i \Lambda_i^{1/2} \boldsymbol{\omega}_i \otimes \boldsymbol{\omega}_i \quad \text{and} \quad \mathbb{C}^{-1/2} = \sum_i \Lambda_i^{-1/2} \boldsymbol{\omega}_i \otimes \boldsymbol{\omega}_i, \tag{8}$$

where Λ_i are the eigenvalues of $\mathbb{C}$, and $\boldsymbol{\omega}_i$ are second-order orthonormal eigentensors associated to Λ_i.

In the case of an isotropic material, $\mathbb{C}^{1/2}$ and $\mathbb{C}^{-1/2}$ are specified by

$$\mathbb{C}^{1/2} = \begin{bmatrix} \sqrt{\frac{\kappa}{2}} + \sqrt{\frac{\mu}{2}} & \sqrt{\frac{\kappa}{2}} - \sqrt{\frac{\mu}{2}} & 0 \\ \sqrt{\frac{\kappa}{2}} - \sqrt{\frac{\mu}{2}} & \sqrt{\frac{\kappa}{2}} + \sqrt{\frac{\mu}{2}} & 0 \\ 0 & 0 & \sqrt{2\mu} \end{bmatrix} \quad \text{and} \quad \mathbb{C}^{-1/2} = \begin{bmatrix} \frac{1}{2\sqrt{2\kappa}} + \frac{1}{2\sqrt{2\mu}} & \frac{1}{2\sqrt{2\kappa}} - \frac{1}{2\sqrt{2\mu}} & 0 \\ \frac{1}{2\sqrt{2\kappa}} - \frac{1}{2\sqrt{2\mu}} & \frac{1}{2\sqrt{2\kappa}} + \frac{1}{2\sqrt{2\mu}} & 0 \\ 0 & 0 & \frac{1}{\sqrt{2\mu}} \end{bmatrix}. \tag{9}$$

Several explicit formulations can be found in[37] to compute these two square root tensors for different types of material. However, it should be noticed that $\mathbb{C}^{1/2}$ and $\mathbb{C}^{-1/2}$ have to be evaluated only once during the simulation.

Following[37], we define the transformed strain tensors $\tilde{\boldsymbol{\varepsilon}} = \mathbb{C}^{1/2} : \boldsymbol{\varepsilon}$. Then, the split decomposition is performed on this new space, implying $\tilde{\boldsymbol{\varepsilon}} = \tilde{\boldsymbol{\varepsilon}}^{+} + \tilde{\boldsymbol{\varepsilon}}^{-}$, in which $\tilde{\boldsymbol{\varepsilon}}^{\pm}$ can be determined via the following expression

$$\tilde{\boldsymbol{\varepsilon}}^{\pm} = \langle \tilde{\varepsilon}_1 \rangle_{\pm} \tilde{\mathbf{E}}_1 + \langle \tilde{\varepsilon}_2 \rangle_{\pm} \tilde{\mathbf{E}}_2 + \langle \tilde{\varepsilon}_3 \rangle_{\pm} \tilde{\mathbf{E}}_3 \tag{10}$$

where the functions $\langle . \rangle_+$ and $\langle . \rangle_-$ are defined by $\langle x \rangle_+ = (x + |x|)/2$ and $\langle x \rangle_- = (x - |x|)/2$. In 2D, the transformed strain tensor $\tilde{\boldsymbol{\varepsilon}}$ admits the following spectral decomposition

$$\tilde{\boldsymbol{\varepsilon}} = \tilde{\varepsilon}_1 \tilde{\mathbf{E}}_1 + \tilde{\varepsilon}_2 \tilde{\mathbf{E}}_2. \tag{11}$$

The eigenvalues $\tilde{\varepsilon}_i$ and eigenprojectors $\tilde{\mathbf{E}}_i$ can be expressed in closed form following the methods proposed by He and Shao[23]. For the case of $\tilde{\varepsilon}_1 \neq \tilde{\varepsilon}_2$, the eigenvalues of the strain tensor can simply be calculated by

$$\tilde{\varepsilon}_1 = \frac{I_1 + (I_1^2 - 4I_2)^{1/2}}{2}, \quad \text{and} \quad \tilde{\varepsilon}_2 = \frac{I_1 - (I_1^2 - 4I_2)^{1/2}}{2}. \tag{12}$$

Above, I_1 and I_2 are the principal invariants of the two-dimensional transformed strain tensor $\tilde{\boldsymbol{\varepsilon}}$

$$I_1 = \operatorname{tr} \tilde{\boldsymbol{\varepsilon}}, \qquad I_2 = \det \tilde{\boldsymbol{\varepsilon}}. \tag{13}$$

In the case of $\tilde{\varepsilon}_1 \neq \tilde{\varepsilon}_2$, then

$$\tilde{\mathbf{E}}_1 = \frac{\tilde{\boldsymbol{\varepsilon}} - \tilde{\varepsilon}_2 \mathbf{1}}{\tilde{\varepsilon}_1 - \tilde{\varepsilon}_2}, \quad \text{and} \quad \tilde{\mathbf{E}}_2 = \mathbf{1} - \tilde{\mathbf{E}}_2. \tag{14}$$

In the case of $\tilde{\varepsilon}_1 = \tilde{\varepsilon}_2$, it implies $\tilde{\boldsymbol{\varepsilon}} = \tilde{\varepsilon}_1 \mathbf{1}$, and

$$\tilde{\mathbf{E}}_1 = [1\ 0;\ 0\ 0] \quad \text{and} \quad \tilde{\mathbf{E}}_2 = [0\ 0;\ 0\ 1]. \tag{15}$$

Once $\tilde{\boldsymbol{\varepsilon}}^{\pm}$ have been obtained, we compute $\boldsymbol{\varepsilon}^{\pm}$ by

$$\boldsymbol{\varepsilon}^{\pm} = \mathbb{C}^{-1/2} : \tilde{\boldsymbol{\varepsilon}}^{\pm}. \tag{16}$$

As demonstrated by He[37], since the positive/negative parts of the transformed strain $\tilde{\boldsymbol{\varepsilon}}^{\pm}$ are orthogonal $\tilde{\boldsymbol{\varepsilon}}^{+} : \tilde{\boldsymbol{\varepsilon}}^{-} = 0$, the extensive and compressive parts obtained by Eq. (16) satisfy the orthogonality condition (7).

The derivatives of $\tilde{\boldsymbol{\varepsilon}}^{\pm}$ with respect to the transformed strain tensor $\tilde{\boldsymbol{\varepsilon}}$ also define two projection tensors $\tilde{\mathbb{P}}^{\pm}(\tilde{\boldsymbol{\varepsilon}}) = \partial_{\tilde{\boldsymbol{\varepsilon}}}\left[\tilde{\boldsymbol{\varepsilon}}^{\pm}(\tilde{\boldsymbol{\varepsilon}})\right]$. It is worth mentioning that the projection tensors can be directly computed from the eigenvalues and eigenprojectors i.e. $\tilde{\mathbb{P}}^{\pm} = f(\tilde{\varepsilon}_i, \tilde{\mathbf{E}}_i)$. As compared to the scheme proposed by Miehe et al.[8], the present model does not require the numerical evaluation of eigenvectors of the strain tensor (see[8,10,38,39,40], and many others). In these papers, the eigenvectors are determined numerically, which is computationally expensive. In the present method, the projection tensors and the positive/negative parts of strain are directly computed from the eigenvalues and eigenprojectors by using their analytical explicit expressions. Hence, the computational efficiency is actually improved. This implies the complete formulation for the proposed decomposition scheme as follows

$$\boldsymbol{\varepsilon}^{\pm} = \left[\mathbb{C}^{-1/2} : \left(\tilde{\mathbb{P}}^{\pm} : \mathbb{C}^{1/2}\right)\right] : \boldsymbol{\varepsilon}. \tag{17}$$

The formulation for the three-dimensional problem can be found in[37]. The Cauchy stress $\boldsymbol{\sigma}$ can be obtained as

$$\boldsymbol{\sigma}(\boldsymbol{\varepsilon}, d) = g(d)\,\frac{\partial \psi^{e+}(\boldsymbol{\varepsilon})}{\partial \boldsymbol{\varepsilon}} + \frac{\partial \psi^{e-}(\boldsymbol{\varepsilon})}{\partial \boldsymbol{\varepsilon}} = \mathbb{C}(d) : \boldsymbol{\varepsilon}. \tag{18}$$

From (17) and by introducing $\mathbb{P}^{\pm} = \mathbb{C}^{-1/2} : \left(\tilde{\mathbb{P}}^{\pm} : \mathbb{C}^{1/2}\right)$, the general form of the elastic tensor accounting for damage is defined by

$$\mathbb{C}(d) = g(d)\,\mathbb{P}^{+} : \mathbb{C} : \mathbb{P}^{+} + \mathbb{P}^{-} : \mathbb{C} : \mathbb{P}^{-}. \tag{19}$$

3 | NUMERICAL IMPLEMENTATION

3.1 | Weak forms

The variational approach to fracture as proposed in Bourdin, Francfort and Marigo[1,2,3] is used here. The employed numerical strategy consists in a series of alternate minimizations, that is minimization with respect to $\mathbf{u}$ at a fixed d and then minimization with respect to d at a fixed $\mathbf{u}$. The details of the proposed minimization procedure is described below.

The mechanical problem is derived by minimizing the total energy with respect to displacements

$$\mathbf{u}(\mathbf{x}) = \operatorname{Arg}\left\{\inf_{\mathbf{u}\in\mathcal{S}_u}\left(E(\mathbf{u}, d) - W^{ext}\right)\right\}, \tag{20}$$

where $\mathcal{S}_u = \left\{\mathbf{u}|\mathbf{u}(\mathbf{x}) = \bar{\mathbf{u}} \text{ on } \partial\Omega_u,\ \mathbf{u} \in H^1(\Omega)\right\}$ and $W^{ext} = \int_\Omega \mathbf{f}\cdot\mathbf{u}\,\mathrm{d}\Omega + \int_{\partial\Omega_F}\overline{\mathbf{F}}\cdot\mathbf{u}\,\mathrm{d}\Gamma$ with $\mathbf{f}$ and $\overline{\mathbf{F}}$ being body forces and prescribed traction over the boundary $\partial\Omega_F$. We obtain the weak form for $\mathbf{u}(\mathbf{x}) \in \mathcal{S}_u$ as follows

$$\int_\Omega \boldsymbol{\sigma} : \boldsymbol{\varepsilon}(\delta\mathbf{u})\,\mathrm{d}\Omega - \int_\Omega \mathbf{f}\cdot\delta\mathbf{u}\,\mathrm{d}\Omega - \int_{\partial\Omega_F}\overline{\mathbf{F}}\cdot\delta\mathbf{u}\,\mathrm{d}\Gamma = 0. \tag{21}$$

The phase field problem consists in minimizing the total energy with respect to phase field

$$d(\mathbf{x}) = \operatorname{Arg}\left\{\inf_{d\in\mathcal{S}_d} E(\mathbf{u}, d)\right\}, \tag{22}$$

where $\mathcal{S}_d = \left\{\nabla d\cdot\mathbf{n} = 0 \text{ on } \partial\Omega, d|\dot{d}(\mathbf{x}) \geq 0, 0 \leq d(\mathbf{x}) \leq 1\right\}$. The evolution law of the phase field to ensure the irreversibility of the process is derived through a thermodynamically consistent framework, see e.g.[11,41,42] for more details. The weak form of the phase field problem is written as

$$\int_\Omega 2\,(1-d)\,\delta d\;\psi^{e+}\,\mathrm{d}\Omega - \int_\Omega \frac{3g_c}{4\ell}\left(\frac{\delta d}{2} + \ell^2\nabla d\nabla\delta d\right)\,\mathrm{d}\Omega = 0. \tag{23}$$

Following Miehe et al.[8], the local crack driving force $\mathcal{H}(\mathbf{x},t)$ is introduced as a dependence on loading history, to take into account loading-unloading:

$$\mathcal{H}(\mathbf{x},t) = \max_{\tau\in[0,t]} \left\{ \frac{\ell}{g_c}\psi^{e+}(\mathbf{x},\tau) \right\}. \tag{24}$$

The weak form of the phase field problem is finally rewritten as

$$\int_\Omega 2\mathcal{H} d\delta d \, \mathrm{d}\Omega + \int_\Omega \frac{3}{4}\ell^2 \nabla d \nabla \delta d \, \mathrm{d}\Omega = \int_\Omega \left\langle 2\mathcal{H} - \frac{3}{8} \right\rangle_+ \delta d \, \mathrm{d}\Omega. \tag{25}$$

3.2 | FEM discretization and staggered solving procedure

The problems described in Eqs. (21), (25) are solved by a standard FE procedure in a staggered procedure (*one pass*), i.e. we alternatively solve the phase field problem and the mechanical problem, see e.g.[8,43,11] for more practical details.

In general, the spectral decomposition of the strain tensor induces a strongly nonlinear mechanical problem. To avoid this nonlinearity, we adopt the shifted strain tensor split algorithms as previously proposed in[11]. Within the present context, the projection tensors defined at time step $n+1$ are approximated as results from the previous time step n, i.e. $\boldsymbol{\varepsilon}^{\pm}_{n+1} \simeq \mathbb{P}^{\pm}(\boldsymbol{\varepsilon}_n) : \boldsymbol{\varepsilon}_{n+1}$. It leads to

$$\mathbb{C}_{n+1}(d) = g(d)\, \mathbb{P}^+(\boldsymbol{\varepsilon}_n) : \mathbb{C} : \mathbb{P}^+(\boldsymbol{\varepsilon}_n) + \mathbb{P}^-(\boldsymbol{\varepsilon}_n) : \mathbb{C} : \mathbb{P}^-(\boldsymbol{\varepsilon}_n). \tag{26}$$

Using the standard FEM discretization, with $\mathbf{N}_u$ and $\mathbf{B}_u$ being vectors of shape functions and matrix of shape functions derivatives of the displacement field, respectively, it yields the following linear system of equations to compute the displacements at time step $n+1$:

$$\mathbf{K}^{uu}_{n+1}\, \mathbf{u}_{n+1} = \mathbf{F}^u_{n+1}, \tag{27}$$

with

$$\mathbf{K}^{uu}_{n+1} = \int_\Omega \mathbf{B}_u^T \mathbf{C}_{n+1}(d) \mathbf{B}_u \, \mathrm{d}\Omega \quad \text{and} \quad \mathbf{F}^u_{n+1} = \int_\Omega \mathbf{N}_u^T \mathbf{f} \, \mathrm{d}\Omega + \int_{\partial\Omega_F} \mathbf{N}_u^T \overline{\mathbf{F}} \, \mathrm{d}\Omega, \tag{28}$$

where $\mathbf{C}_{n+1}(d)$ is the matrix form of the elastic tensor defined in (26) in Voigt's notation.

Using the same standard FEM discretization, with $\mathbf{N}_d$ and $\mathbf{B}_d$ being vector of shape functions and matrix of shape functions derivatives, respectively, it results in the linear system of equations for the phase field problem:

$$\mathbf{K}^d_{n+1}\mathbf{d}_{n+1} = \mathbf{F}^d_{n+1}, \tag{29}$$

with

$$\mathbf{K}^d_{n+1} = \int_\Omega \left(2\mathcal{H}_{n+1}\mathbf{N}_d^T\mathbf{N}_d + \frac{3\ell^2}{4}\mathbf{B}_d^T\mathbf{B}_d \right) \mathrm{d}\Omega \quad \text{and} \quad \mathbf{F}^d_{n+1} = \int_\Omega \left\langle 2\mathcal{H}_{n+1} - \frac{3}{8} \right\rangle_+ \mathbf{N}_d^T \, \mathrm{d}\Omega. \tag{30}$$

4 | NUMERICAL EXAMPLES

4.1 | Comparison of the present scheme with other available models

In the first part of the numerical examples, we will compare the present scheme (SD3) with the two other models, Amor et al.[5] (SD1) and Miehe et al.[8] (SD2) for different characteristic loading which involve self-contact within a crack.

4.1.1 | Single edge notched: pure shear test

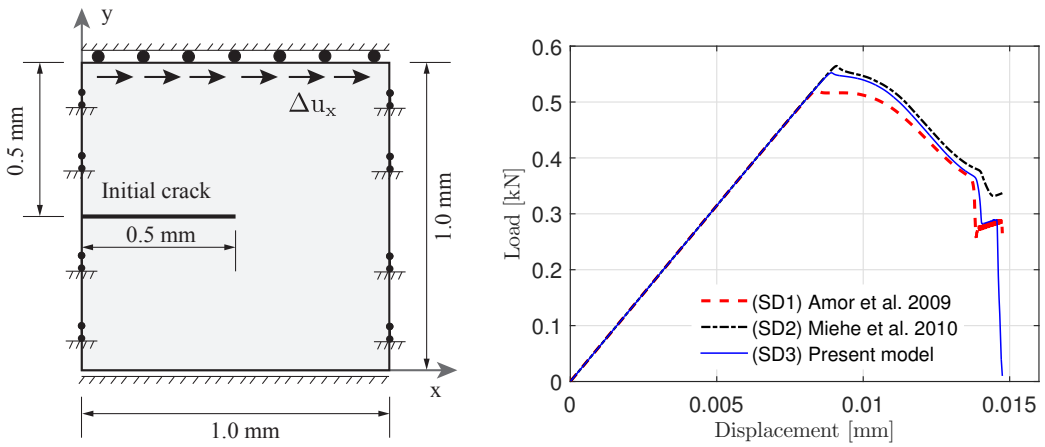

(a) (b)

FIGURE 2 Single edge notched pure shear test sample: (a) geometry and boundary conditions; (b) comparison of load - displacement curves for the different strain split operators. The prediction of the (SD1) model (Amor et al.[5]) is significantly different with respect to the (SD2) and (SD3) models.

The benchmark example of the single edge notched pure shear test discussed in the study of Miehe et al.[8] is considered. A squared plate (1 mm × 1 mm) with an initial horizontal crack placed at a middle height from the left outer surface to the center of the specimen is subjected to a shear load (see Fig. 2 (a)). The structure is meshed with triangular elements with $h_e^{max} = 0.03$ mm and $h_e^{min} = 0.0025$ mm for the critical region of expected crack path. The boundary conditions are as follows: the displacements along y on the whole boundary region and the displacement along x at the lower edge ($y = 0$) mm are fixed to zero. The displacements are prescribed along the $x-$direction for upper edge ($y = 1$) mm. Plane strain condition is assumed.

The material properties are chosen following[8], with the isotropic elastic modulus characterized by Lamé's coefficients $\lambda = 121.15$ GPa, and $\mu = 80.77$ GPa and a critical energy release rate $g_c = 2.7 \times 10^{-3}$ kN/mm. The length scale parameter is chosen as $\ell = 0.0075$ mm. The computation is performed in a monotonic displacement driven context with constant displacement increments of $\Delta u_x = 10^{-5}$ mm for 1500 time steps.

The load-displacement curves for the three models are plotted in Fig. 2(b). Even though the mechanical response in the elastic phase is the same, we observe different fracture behaviors. It shows that the prediction of the present model (SD3) is similar to the one of Miehe et al.[8] (SD2), but significantly different from the one of Amor et al.[5] (SD1) model in this situation. More specifically, the (SD1) model predicts a lower crack initiation stress than those ones of (SD2) and (SD3) models. The reason could be related to the fact that the formulation proposed by Amor et al.[44] allows for the whole deviatoric part of strain creating fracture while the models proposed by Miehe et al.[8], and He and Shao[23] do not. Due to a lack of experimental results, we cannot conclude on which model is more accurate than another. A detailed investigation in both numerical and experimental approaches for various materials is needed to clarify this point and has to be pursued in future works.

More interestingly, at the final stage of crack growth the (SD1) and (SD2) split formulations are able to describe the full degradation of the material due to crack propagation. Especially, only the proposed model (SD3) accurately captures the full fracture behavior (total material resistance loss).

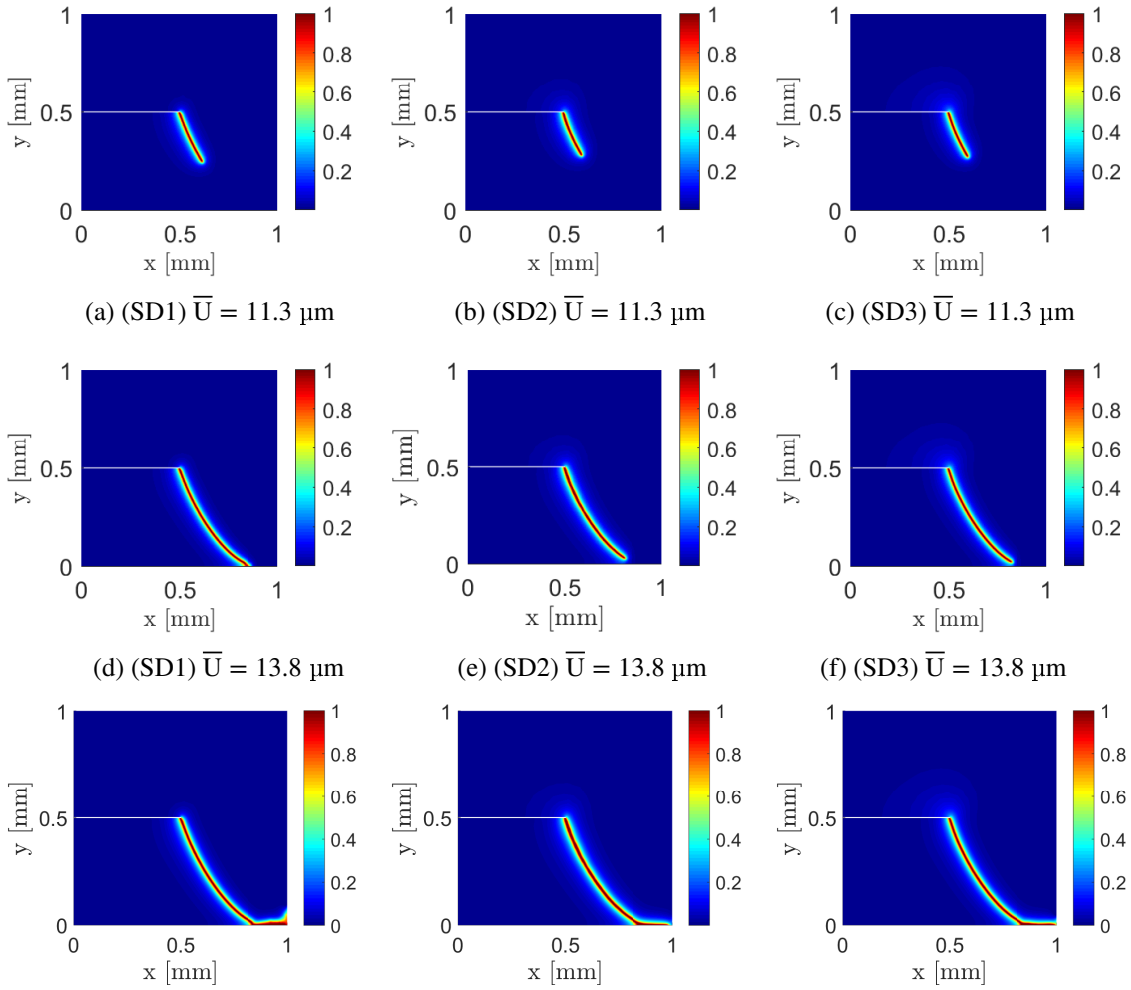

(a) (SD1) $\overline{U} = 11.3$ µm (b) (SD2) $\overline{U} = 11.3$ µm (c) (SD3) $\overline{U} = 11.3$ µm

(d) (SD1) $\overline{U} = 13.8$ µm (e) (SD2) $\overline{U} = 13.8$ µm (f) (SD3) $\overline{U} = 13.8$ µm

(g) (SD1) $\overline{U} = 14.7$ µm (h) (SD2) $\overline{U} = 14.7$ µm (i) (SD3) $\overline{U} = 14.7$ µm

FIGURE 3 Comparison of fracture response predicted by the different models for the shear test.

4.1.2 | Double edge notched: Crack coalescence test

Next, the well-known benchmark test of crack coalescence is studied[45,46]. We consider a square plate with asymmetric double notched, as described in Fig. 4(a). An unstructured mesh, containing 49296 triangular elements, is employed with $h_e^{min} = 0.05$ mm for the critical region of expected crack path. The material parameters are the same as those in the previous example of the pure shear test, except the internal length scale being $\ell = 0.135$ mm. The computation is performed in a monotonic displacement driven context with constant displacement increments $\Delta u_y = 10^{-4}$ mm in the first period and which are adjusted to $\Delta u_x = 2 \times 10^{-5}$ mm as soon as the phase field $d > 0.6$ in one FE node.

We plot the obtained macroscopic curves in Fig. 4(b). In general, the global responses predicted by three different models are nearly the same for the traction test. Again, the (SD1) model gives the lowest load for crack initiation and also the smallest prescribed displacement for collapse of the structure, followed by (SD3) model and then (SD2) model. More interestingly, in this test, the present model (SD3) is close to the (SD1) model of Amor et al.[5] instead of (SD2) model as in the previous case, even though if this effect is very small. This point is demonstrated through a zoom in the load - displacement curve in Fig. 4(b). The behaviors of crack propagation and coalescence are similar for all three cases, as shown in Figs. 5, where we provide the crack paths predicted by different models at the same loading. It is worth mentioning that the numerical results reproduce very well the phenomenon of cracks avoiding each other as noticed in the experimental observation[47], see Figs. 6.

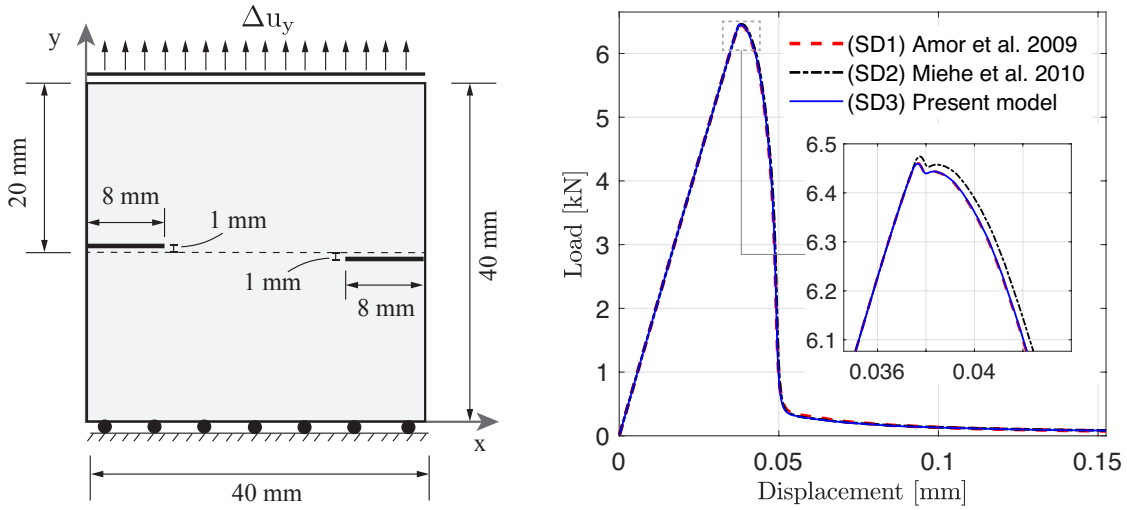

(a) (b)

FIGURE 4 Double edge notched crack coalescence test: (a) geometry and boundary conditions; (b) comparison of load - displacement curves obtained by different models.

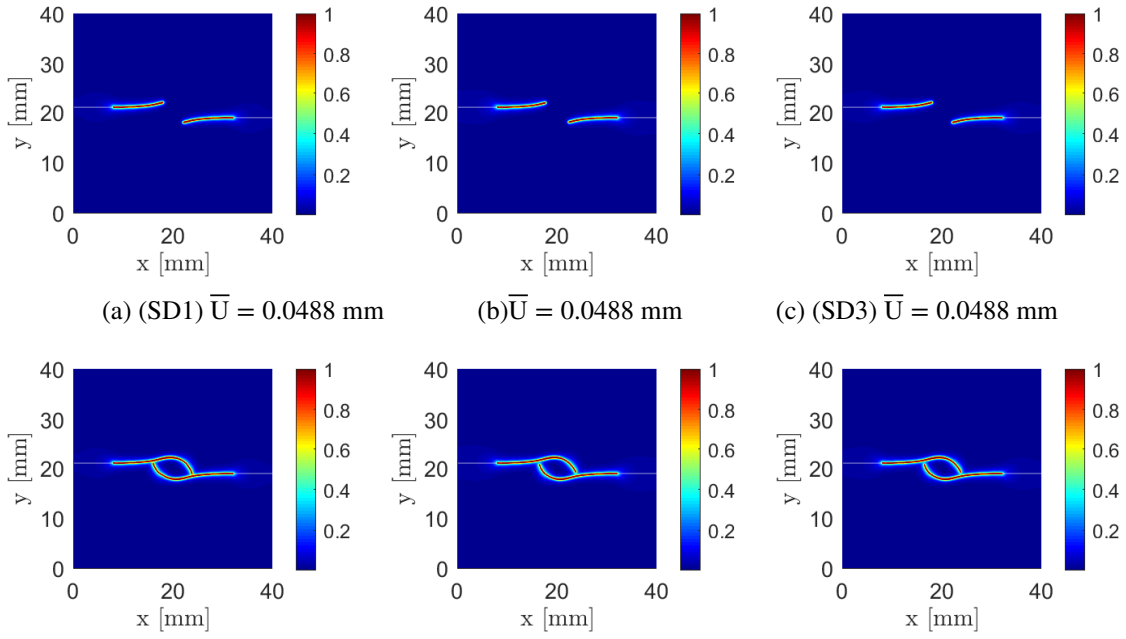

(a) (SD1) $\overline{U} = 0.0488$ mm (b)$\overline{U} = 0.0488$ mm (c) (SD3) $\overline{U} = 0.0488$ mm

(d) (SD1) $\overline{U} = 0.1937$ mm (e) (SD2) $\overline{U} = 0.1937$ mm (f) (SD3) $\overline{U} = 0.1937$ mm

FIGURE 5 Comparison of fracture response predicted by the different models for the case of crack coalescence test.

4.1.3 | Sample containing a hole: Compression test

In this example, we investigate the crack initiation and propagation in a structure containing a hole subjected to compression load. Such problem has been previously investigated experimentally and numerically[48,35]. The geometry of the considered drilled plaster sample is shown in Fig. 7(a).

The model parameters of the plaster material are taken from[35], with elastic modulus $E = 12$ GPa, Poisson's ratio $\nu = 0.3$, critical fracture energy $g_c = 1.4$ N/m, and the internal length scale is chosen as $\ell = 0.12$ mm. 2D plane strain simulation

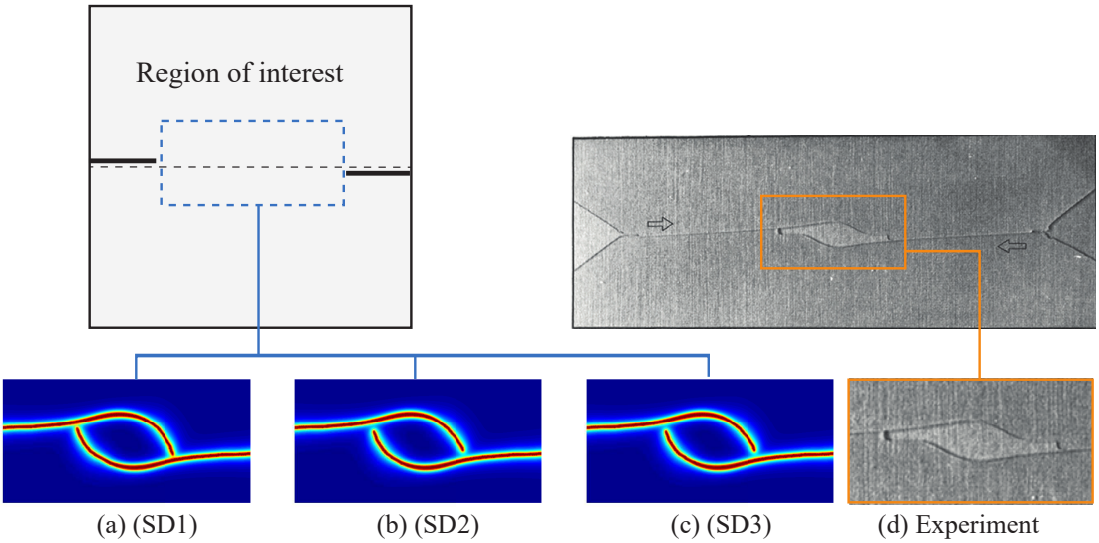

FIGURE 6 Crack coalescence behavior in the traction test of a doubled notched sample. All three models successfully reproduce the phenomenon of cracks avoiding each other observed in the experiment[47].

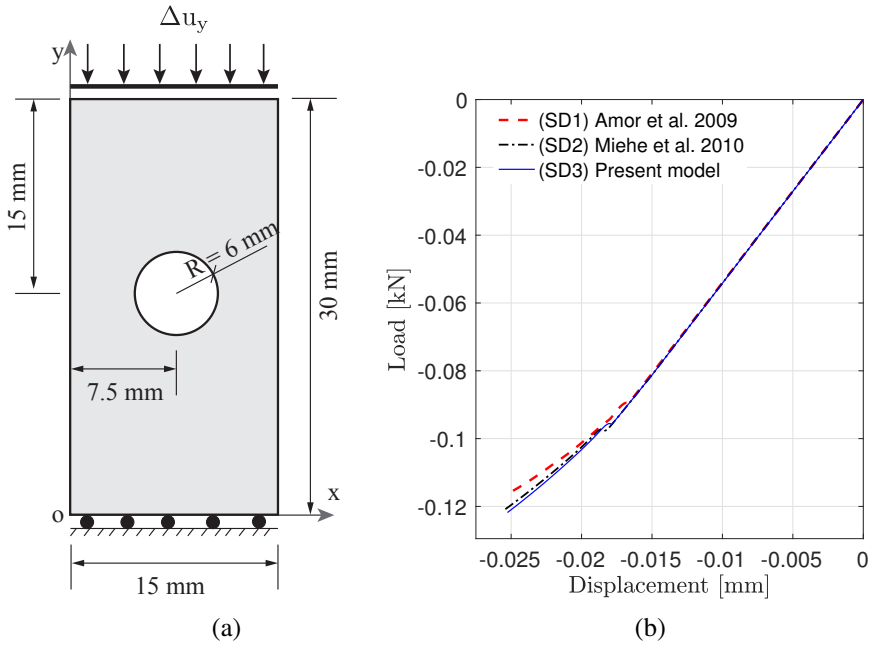

FIGURE 7 Compression test of a sample containing an hole: (a) geometry and boundary conditions; (b) comparison of load - displacement curves for the different models. The (SD1) model again predicts a lower fracture resistance as compared to the (SD2) and (SD3) models.

is conducted. Monotonic compressive displacement increments are prescribed on the top edge of the specimen, with $\Delta u_y = -8 \times 10^{-5}$ mm in the first period and then switch to $\Delta u_y = -2 \times 10^{-5}$ mm as soon as the phase field $d > 0.6$ in one FE node.

The obtained load-displacement curves predicted by three different models are provided in Fig. 7(b). We note that the result of the orthogonal decomposition (SD3) is similar to the one of Miehe et al.[8] (SD2). The (SD1) model again shows a significantly lower mechanical resistance, which can be related to the presence of damage in the shear band localization as depicted in Figs. 8(a)(d). All three models are able to reproduce the vertical crack propagation as predicted by experiments (see[48,35]). However, the (SD1) and (SD2) models induce spurious damage regions at the left and right side of the hole, which are not

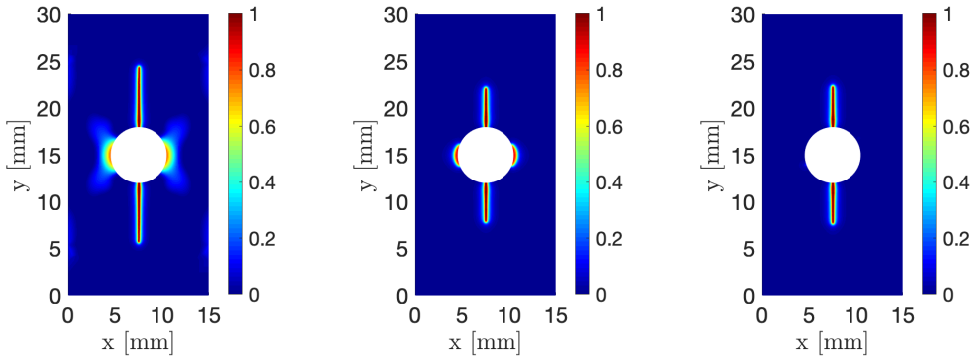

(a) (SD1) $\overline{U} = 18.5$ µm (b) (SD2) $\overline{U} = 18.5$ µm (c) (SD3) $\overline{U} = 18.5$ µm

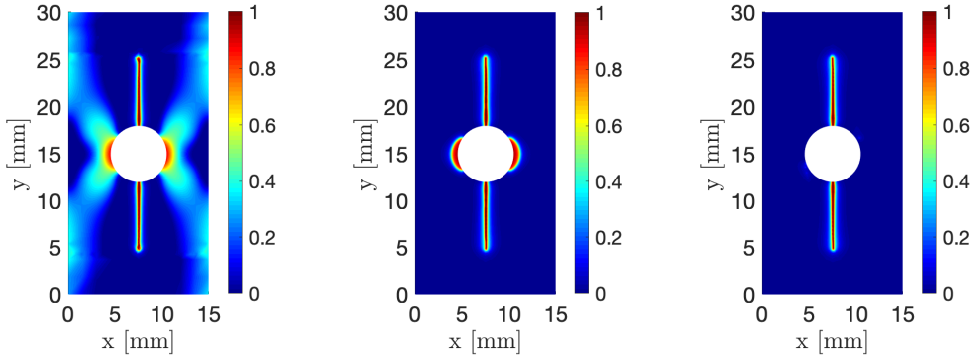

(d) (SD1) $\overline{U} = 24.6$ µm (e) (SD2) $\overline{U} = 24.6$ µm (f) (SD3) $\overline{U} = 24.6$ µm

FIGURE 8 Compressive test: comparison of fracture behaviors predicted by the different models.

observed in the experiments ([48,35]), as shown in Fig. 9. Interestingly, the present model (SD3) does not induce such spurious effect, as shown in Fig. 9(d). It confirms the accuracy of the orthogonal decomposition to simulate the crack initiation and propagation of brittle material under compression load.

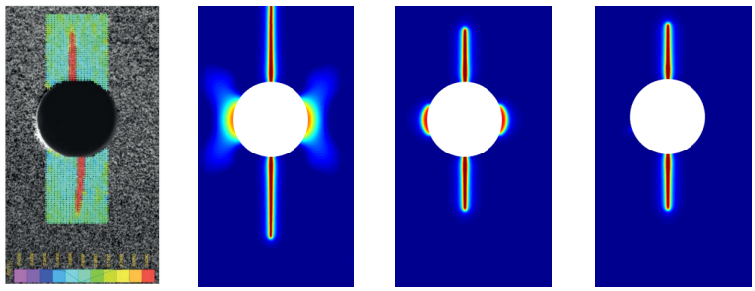

(a) Experiment (b) (SD1) (c) (SD2) (d) (SD3)

FIGURE 9 Compressive test: comparison of crack paths predicted by the different strain decomposition schemes with the one of experiment[48,35] for the same loading.

4.2 | Crack propagation in an initially anisotropic elastic medium, effects of material orientation

The last numerical experiment is dedicated to demonstrate the capacity of the (SD3) to deal with the case of an initially anisotropic elastic medium, e.g. a monocrystal with given orientation. Note that here we do not consider an anisotropic damage model, i.e. taking into account the anisotropy of cracking (see several models in this context, e.g.[49,32,50]. Then, the damage model is isotropic but the elastic medium is anisotropic, inducing effects of the material orientation during crack propagation.

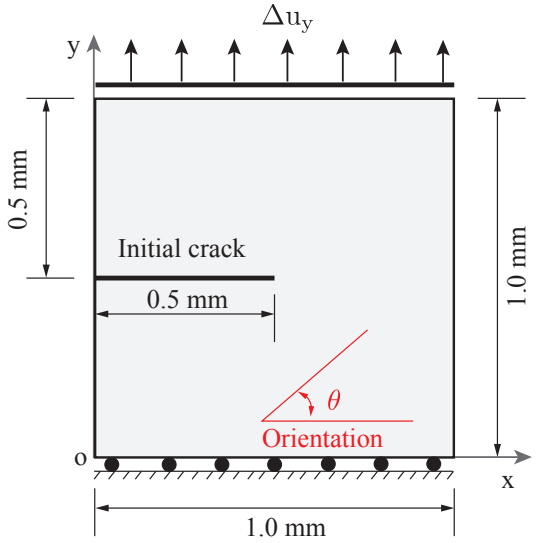

FIGURE 10 Description of the anisotropic media: geometry and boundary conditions.

The same single edge notched sample as in the pure shear test is used. It is subjected to a traction load, see Fig. 10. The components of the elastic stiffness tensor matrix $\mathbf{C}_{(\text{ref})}$ (in Voigt notation) are given in the reference coordinate system as

$$\mathbf{C}_{(\text{ref})} = \begin{bmatrix} 65 & 20 & 0 \\ 20 & 260 & 0 \\ 0 & 0 & 30 \end{bmatrix} [\text{GPa}]. \tag{31}$$

It should be noticed that the existing split operators for the strain tensors models[5,8,31] are unable to apply to such a situation. There is no available formulation for the decomposition following the frame work of Miehe et al.[8] to model such anisotropic/orthotropic material. As described in A, the formulation proposed by Amor et al. (SD1) model requires a definition of the bulk modulus and is thus not able to handle such situation.

The orientation-dependent elastic stiffness tensor with respect to the reference coordinate system is determined by

$$\mathbf{C} = \mathbf{P}^{\mathrm{T}} \mathbf{C}_{(\text{ref})} \mathbf{P}, \tag{32}$$

where $\mathbf{P}$ is the transformation tensor in Voigt's notation. In the general 2D case, the rotation of material orientation can be simply determined following[51] as

$$\mathbf{P} = \begin{bmatrix} c^2 & s^2 & 2cs \\ s^2 & c^2 & -2cs \\ -cs & cs & c^2 - s^2 \end{bmatrix}, \tag{33}$$

where $c = \cos(2\pi - \theta)$, $s = \sin(2\pi - \theta)$, with $2\pi - \theta$ is the Euler angle of material orientation, and θ is the orientation angle with respect to the x-axis, as described in Fig. 10.

We perform 19 simulations corresponding to θ varying from 0° to 90°, with step of 5°, i.e. $\theta = [0°, 5°, 10°, 15°, ..., 90°]$. The critical energy is taken to be independent of the material orientation with $g_c = 10^{-3}$ kN/mm, and the length scale is taken as $\ell = 0.0085$ mm. The computation is performed in a monotonic displacement driven context with constant displacement increments of $\Delta u_y = 6 \times 10^{-5}$ mm in the first period and then adjusted to $\Delta u_y = 2 \times 10^{-5}$ mm as soon as the phase field $d > 0.6$ in one FE node.

In order to evaluate the effects of material orientation, we define the normalized maximum principal stresses near the crack tip by

$$\sigma_{\mathrm{Nlz}}(r,\varphi) = \frac{\overline{\sigma}(r,\varphi)}{\overline{\sigma}_{\max}}, \tag{34}$$

where r, φ are the polar coordinates with origin at the crack tip; $\overline{\sigma}(r,\varphi) = \max(\sigma_1(r,\varphi), \sigma_2(r,\varphi))$; and $\overline{\sigma}_{\max}$ is the maximal value of $\overline{\sigma}(r,\varphi)$ over the considered region.

The plots of $\sigma_{\mathrm{Nlz}}(r,\varphi)$ at $r = 0.035$ mm are provided in Fig. 11 for the elastic phase and in Fig. 12 after crack initiation. The obtained crack paths corresponding to different material orientations are depicted in Fig. 13. The effects of the directional dependence of material properties are captured. Instead of purely propagating along the horizontal direction, the crack also propagates in other directions depending on the competition between guided load and guided material cleavage plan. The crack orientation occurs in a direction perpendicular to the greatest tensile stress at the elastic phase. Note again that these effects are small as we did not introduce here an anisotropic damage model through the fracture energy term, but only an isotropic damage interacting with an initially anisotropic elastic medium.

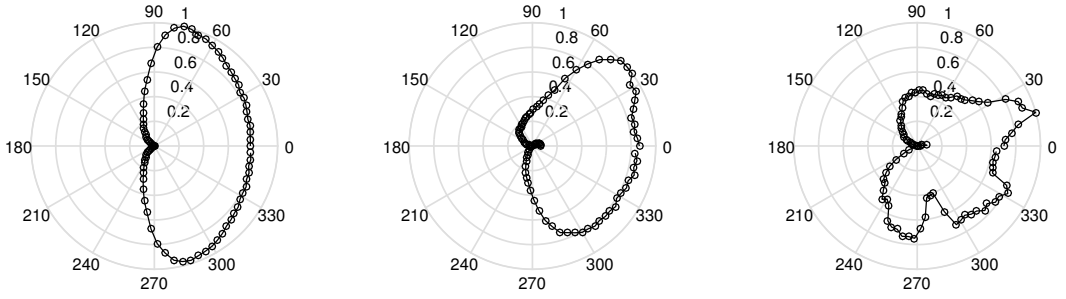

(a) Material orientation $\theta = 0°$ (b) Material orientation $\theta = 10°$ (c) Material orientation $\theta = 60°$

FIGURE 11 Polar plot of the normalized maximum principal stresses $\sigma_{\mathrm{Nlz}}(r,\varphi)$ near the crack tip at $r = 0.035$ mm for the same loading $\overline{\mathrm{U}} = 4$ µm. The crack onset and propagation occurs in a direction perpendicular to the greatest tensile stress.

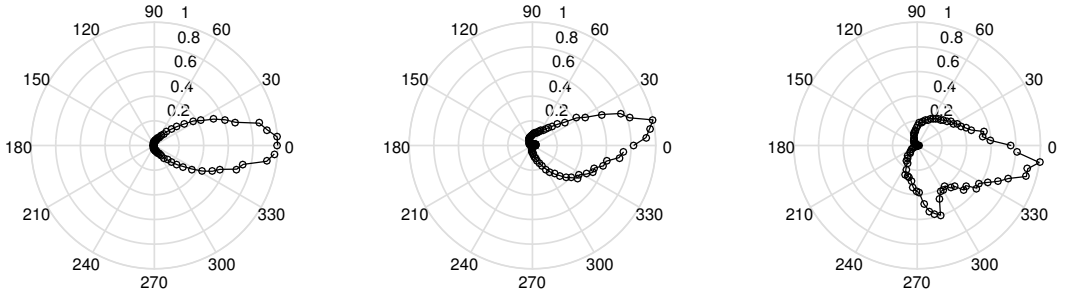

(a) Material orientation $\theta = 0°$ (b) Material orientation $\theta = 10°$ (c) Material orientation $\theta = 60°$

FIGURE 12 Polar plot of the normalized maximum principal stresses $\sigma_{\mathrm{Nlz}}(r,\varphi)$ near the crack tip at $r = 0.035$ mm after crack initiation. The peak of the stress concentration depicts the direction of crack propagation.

We provide the global loading curves as well as the maximal overall stress (peak stress in the loading curves), and the overall fracture resistance (area under the loading curves) in Figs. 14. The anisotropic effects strongly alter the mechanical response

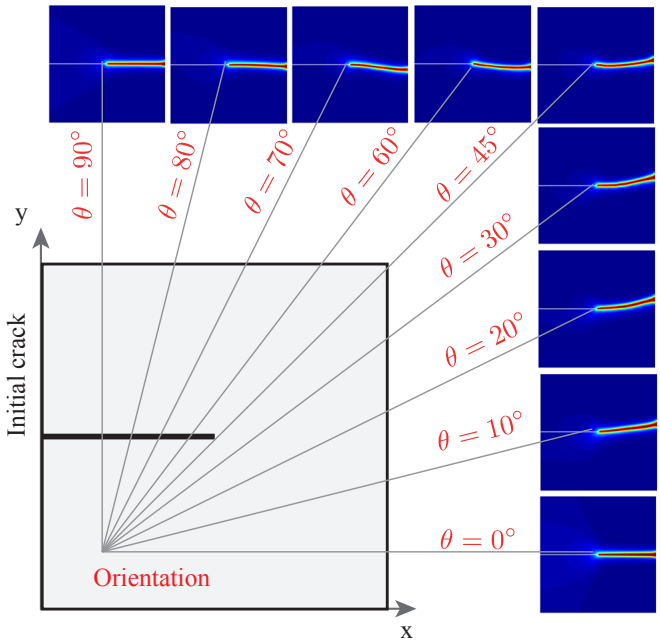

FIGURE 13 Cracks for different material orientation angles obtained by the orthogonal decomposition scheme SD3.

and fracture behavior. We observe that the mechanical performance of the material reaches its maximal state at the orientation $\theta = 0°$, and its minimal value at $\theta = 45°$.

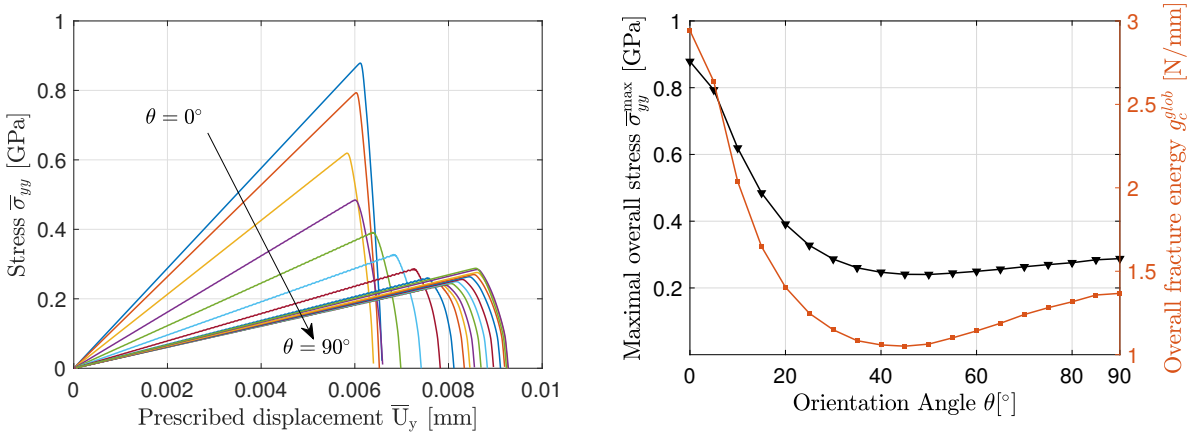

(a) Load - displacements curves (b) Mechanical performance

FIGURE 14 Comparison of the mechanical responses for different orientation angles: the material anisotropic effects are clearly captured. The material orientation strongly alters the mechanical performance as demonstrated by the pic stress and the global fracture energy

5 | CONCLUSION

In this work, we have used the new orthogonal split of the strain tensor proposed by [23] in the phase field model. Projection tensors have been introduced and numerical implementation details have been provided. Comparisons with other schemes have shown

a good agreement with other models in most situations. The advantage as compared to other available strain split operators are: (a) the possibility of dealing with any arbitrary initial anisotropic behavior; (b) an efficient numerical implementation due to very simple closed forms of projection operators and (c) a strict orthogonality between the traction and compression parts of the strain tensor, which seems to remove some spurious effects in crack propagation under compression loads.

ACKNOWLEDGMENTS

This research is supported by the project SeRaMCo within the program INTERREG – NWE.

References

1. Francfort G, Marigo J. Revisiting brittle fracture as an energy minimization problem. *Journal of the Mechanics and Physics of Solids* 1998; 46(8): 1319–1342.

2. Bourdin B, Francfort G, Marigo J. Numerical experiments in revisited brittle fracture. *Journal of the Mechanics and Physics of Solids* 2000; 48(4): 797–826.

3. Bourdin B, Francfort G, Marigo J. The variational approach to fracture. *Journal of Elasticity* 2008; 91(1-3): 5–148.

4. Karma A, Kessler D, Levine H. Phase-field model of mode III dynamic fracture. *Physical Review Letters* 2001; 87(4): 45501.

5. Amor H, Marigo J, Maurini C. Regularized formulation of the variational brittle fracture with unilateral contact: Numerical experiments. *Journal of the Mechanics and Physics of Solids* 2009; 57(8): 1209–1229.

6. Hakim V, Karma A. Laws of crack motion and phase-field models of fracture. *Journal of the Mechanics and Physics of Solids* 2009; 57(2): 342–368.

7. Kuhn C, Müller R. A continuum phase field model for fracture. *Engineering Fracture Mechanics* 2010; 77(18): 3625–3634.

8. Miehe C, Hofacker M, Welschinger F. A phase field model for rate-independent crack propagation: Robust algorithmic implementation based on operator splits. *Computer Methods in Applied Mechanics and Engineering* 2010; 199: 2765–2778.

9. Bourdin B, Larsen C, Richardson C. A time-discrete model for dynamic fracture based on crack regularization. *International Journal of Fracture* 2011; 168: 133-143.

10. Borden M, Verhoosel C, Scott M, Hughes T, Landis C. A phase-field description of dynamic brittle fracture. *Computer Methods in Applied Mechanics and Engineering* 2012; 217: 77–95.

11. Nguyen T, Yvonnet J, Zhu QZ, Bornert M, Chateau C. A phase field method to simulate crack nucleation and propagation in strongly heterogeneous materials from direct imaging of their microstructure. *Engineering Fracture Mechanics* 2015; 139: 18–39.

12. Ortiz M. A constitutive theory for the inelastic behavior of concrete. *Mechanics of materials* 1985; 4(1): 67–93.

13. Simo J, Ju J. Strain-and stress-based continuum damage models—I. Formulation. *International Journal of Solids and Structures* 1987; 23(7): 821–840.

14. Mazars J, Pijaudier-Cabot G. Continuum damage theory—application to concrete. *Journal of Engineering Mechanics* 1989; 115(2): 345–365.

15. Ju J. Isotropic and anisotropic damage variables in continuum damage mechanics. *Journal of Engineering Mechanics* 1990; 116(12): 2764–2770.

16. Ramtani S, Berthaud Y, Mazars J. Orthotropic behavior of concrete with directional aspects: modelling and experiments. *Nuclear Engineering and Design* 1992; 133(1): 97–111.

17. Hansen N, Schreyer H. A thermodynamically consistent framework for theories of elastoplasticity coupled with damage. *International Journal of Solids and Structures* 1994; 31(3): 359–389.

18. Papa E, Taliercio A. Anisotropic damage model for the multiaxial static and fatigue behaviour of plain concrete. *Engineering Fracture Mechanics* 1996; 55(2): 163–179.

19. Cervera M, Oliver J, Faria R. Seismic evaluation of concrete dams via continuum damage models. *Earthquake engineering & structural dynamics* 1995; 24(9): 1225–1245.

20. Comi C, Perego U. Fracture energy based bi-dissipative damage model for concrete. *International Journal of Solids and Structures* 2001; 38(36-37): 6427–6454.

21. Giacomini A, Ponsiglione M. Non-interpenetration of matter for SBV deformations of hyperelastic brittle materials. *Proceedings of the Royal Society of Edinburgh Section A: Mathematics* 2008; 138(5): 1019–1041.

22. Wu J, Cervera M. A novel positive/negative projection in energy norm for the damage modeling of quasi-brittle solids. *International Journal of Solids and Structures* 2018; 139: 250–269.

23. He QC, Shao Q. Closed-Form Coordinate-Free Decompositions of the Two-Dimensional Strain and Stress for Modeling Tension–Compression Dissymmetry. *Journal of Applied Mechanics* 2019; 86(3): 031007.

24. Henry H, Levine H. Dynamic instabilities of fracture under biaxial strain using a phase field model. *Physical Review Letters* 2004; 93(10): 105504.

25. Piero GD, Lancioni G, March R. A variational model for fracture mechanics: numerical experiments. *Journal of the Mechanics and Physics of Solids* 2007; 55(12): 2513–2537.

26. Lancioni G, Royer-Carfagni G. The variational approach to fracture mechanics. A practical application to the French Panthéon in Paris. *Journal of elasticity* 2009; 95(1-2): 1–30.

27. Freddi F, Royer-Carfagni G. Regularized variational theories of fracture: a unified approach. *Journal of the Mechanics and Physics of Solids* 2010; 58(8): 1154–1174.

28. Ambati M, Gerasimov T, Lorenzis LD. A review on phase-field models of brittle fracture and a new fast hybrid formulation. *Computational Mechanics* 2015; 55(2): 383–405.

29. Li T, Marigo JJ, Guilbaud D, Potapov S. Gradient damage modeling of brittle fracture in an explicit dynamics context. *International Journal for Numerical Methods in Engineering* 2016; 108(11): 1381–1405.

30. Miehe C. Comparison of two algorithms for the computation of fourth-order isotropic tensor functions. *Computers & Structures* 1998; 66(1): 37–43.

31. Clayton J, Knap J. Phase field modeling of directional fracture in anisotropic polycrystals. *Computational Materials Science* 2015; 98: 158–169.

32. Nguyen T, Réthoré J, Yvonnet J, Baietto MC. Multi-phase-field modeling of anisotropic crack propagation for polycrystalline materials. *Computational Mechanics* 2017; 60: 289–314.

33. Ambrosio L, Tortorelli V. Approximation of functional depending on jumps by elliptic functional via Γ-convergence. *Communications on Pure and Applied Mathematics* 1990; 43(8): 999–1036.

34. Pham K, Amor H, Marigo JJ, Maurini C. Gradient damage models and their use to approximate brittle fracture. *International Journal of Damage Mechanics* 2011; 20(4): 618–652.

35. Nguyen T, Yvonnet J, Bornert M, et al. On the choice of parameters in the phase field method for simulating crack initiation with experimental validation. *International Journal of Fracture* 2016; 197(2): 213–226.

36. Nguyen T, Yvonnet J, Bornert M, Chateau C. Initiation and propagation of complex 3D networks of cracks in heterogeneous quasi-brittle materials: Direct comparison between in situ testing-microCT experiments and phase field simulations. *Journal of the Mechanics and Physics of Solids* 2016; 95: 320 - 350.

37. He QC. Three-Dimensional Strain and Stress Orthogonal Decompositions Via an Elastic Energy Preserving Transformation. 2018.

38. Hesch C, Weinberg K. Thermodynamically consistent algorithms for a finite-deformation phase-field approach to fracture. *International Journal for Numerical Methods in Engineering* 2014; 99(12): 906–924.

39. Ambati M, Gerasimov T, Lorenzis LD. Phase-field modeling of ductile fracture. *Computational Mechanics* 2015; 55(5): 1017–1040.

40. Lee S, Wheeler M, Wick T. Pressure and fluid-driven fracture propagation in porous media using an adaptive finite element phase field model. *Computer Methods in Applied Mechanics and Engineering* 2016; 305: 111–132.

41. Nguyen T, Yvonnet J, Zhu QZ, Bornert M, Chateau C. A phase-field method for computational modeling of interfacial damage interacting with crack propagation in realistic microstructures obtained by microtomography. *Computer Methods in Applied Mechanics and Engineering* 2016; 312: 567 - 595.

42. Nguyen T, Yvonnet J, Waldmann D, He Q. Phase field modeling of interfacial damage in heterogeneous media with stiff and soft interphases. 2019; 218: 106574.

43. Miehe C, Schänzel LM, Ulmer H. Phase field modeling of fracture in multi-physics problems. Part I. Balance of crack surface and failure criteria for brittle crack propagation in thermo-elastic solids. *Computer Methods in Applied Mechanics and Engineering* 2015; 294: 449–485.

44. Amin M, Kim JS, Lee Y, Kim JK. Simulation of the thermal stress in mass concrete using a thermal stress measuring device. *Cement and Concrete Research* 2009; 39(3): 154–164.

45. Sumi Y, Wang Z. A finite-element simulation method for a system of growing cracks in a heterogeneous material. *Mechanics of Materials* 1998; 28(1-4): 197–206.

46. Moës N, Stolz C, Bernard P, Chevaugeon N. A level set based model for damage growth: the thick level set approach. *International Journal for Numerical Methods in Engineering* 2011; 86(3): 358–380.

47. Melin S. Why do cracks avoid each other?. *International Journal of Fracture* 1983; 23(1): 37–45.

48. Romani R, Bornert M, Leguillon D, Roy RL, Sab K. Detection of crack onset in double cleavage drilled specimens of plaster under compression by digital image correlation-Theoretical predictions based on a coupled criterion. *European Journal of Mechanics - A/Solids* 2015; 51: 172–182.

49. Nguyen T, Réthoré J, Baietto MC. Phase field modelling of anisotropic crack propagation. *European Journal of Mechanics-A/Solids* 2017; 65: 279–288.

50. Bleyer J, Alessi R. Phase-field modeling of anisotropic brittle fracture including several damage mechanisms. *Computer Methods in Applied Mechanics and Engineering* 2018; 336: 213–236.

51. Li B, Peco C, Millán D, Arias I, Arroyo M. Phase-field modeling and simulation of fracture in brittle materials with strongly anisotropic surface energy. *International Journal for Numerical Methods in Engineering* 2015; 102(3-4): 711–727.

APPENDIX

A REVIEW OF OTHER AVAILABLE SPLIT OPERATORS FOR THE STRAIN TENSOR

A.1 (SD1) Volumetric/deviatoric decomposition of the strain proposed by Amor et al.[5].

In[5], the elastic strain is decomposed into spherical $\boldsymbol{\varepsilon}^{\text{sph}}$ and deviatoric $\boldsymbol{\varepsilon}^{\text{dev}}$ parts, with $\boldsymbol{\varepsilon} = \boldsymbol{\varepsilon}^{\text{sph}} + \boldsymbol{\varepsilon}^{\text{dev}}$. Then, it is assumed that the damage is created by expansion only (positive spherical part) and shear

$$\psi^e = \begin{cases} \dfrac{1}{2} g(d_i) \big[\boldsymbol{\varepsilon} : \mathbb{C}^0 : \boldsymbol{\varepsilon} \big] & \text{if } \operatorname{tr} \boldsymbol{\varepsilon} \geq 0, \\ \dfrac{1}{2} \big[\boldsymbol{\varepsilon}^{\text{sph}} : \mathbb{C}^0 : \boldsymbol{\varepsilon}^{\text{sph}} \big] + \dfrac{1}{2} g(d) \big[\boldsymbol{\varepsilon}^{\text{dev}} : \mathbb{C}^0 : \boldsymbol{\varepsilon}^{\text{dev}} \big] & \text{if } \operatorname{tr} \boldsymbol{\varepsilon} < 0. \end{cases} \tag{A1}$$

By introducing the bulk modulus k_0 for the undamaged material (relating the spherical part of the strain to the spherical part of the stress), the elastic tensor is now written as:

$$\mathbb{C}(\boldsymbol{d}) = g(\boldsymbol{d}) \mathbb{C}^0 + k_0 \mathbf{1} \otimes \mathbf{1} \big[1 - g(\boldsymbol{d}) \big] \operatorname{sign}^-(\operatorname{tr} \boldsymbol{\varepsilon}^e), \tag{A2}$$

where the sign function $\operatorname{sign}^-(x) = 1$ if $x < 0$ and $\operatorname{sign}^-(x) = 0$ if $x \geq 0$. The strain energy can be now rewritten as:

$$\psi^e(\boldsymbol{\varepsilon}, d) = \frac{1}{2} \big[\boldsymbol{\varepsilon} : \mathbb{C}(\boldsymbol{d}) : \boldsymbol{\varepsilon} \big]. \tag{A3}$$

The (SD1) model is able to simulate the isotropic material and several kinds of material symmetry such as cubic, hexagonal, or trigonal symmetry. It is unable to describe the behavior of an arbitrary anisotropic material.

A.2 (SD2) Extensive/compressive decomposition of the strain proposed by Miehe et al.[8].

In[8], the elastic strain is decomposed into extensive $\boldsymbol{\varepsilon}^+$ and compressive $\boldsymbol{\varepsilon}^-$ parts, with $\boldsymbol{\varepsilon} = \boldsymbol{\varepsilon}^+ + \boldsymbol{\varepsilon}^-$. Then, it is assumed that the damage is created by traction only

$$\psi^{e\pm}(\boldsymbol{\varepsilon}) = \frac{\lambda}{2} \big[\langle \operatorname{tr} \boldsymbol{\varepsilon} \rangle_{\pm} \big]^2 + \mu \operatorname{tr} \big[\big(\boldsymbol{\varepsilon}^{\pm} \big)^2 \big], \tag{A4}$$

where $\langle x \rangle_+$ is the positive operator, with $\langle x \rangle_+ = x$ if $x \geq 0$, and $\langle x \rangle_+ = 0$ if $x < 0$. Conversely, $\langle x \rangle_-$ is the negative operator, with $\langle x \rangle_- = 0$ if $x \geq 0$, and $\langle x \rangle_+ = x$ if $x < 0$.

The (SD2) model is only able to simulate damage in initially isotropic elastic materials. There is no available formulation for anisotropic materials according the author's best knowledge.